Diffusion MRS tracks distinct trajectories of neuronal development in the cerebellum and thalamus of rat neonates.

Clémence Ligneul[1]✉, Lily Qiu[1], William T Clarke[1], Saad Jbabdi[1], Marco Palombo[2,3]*, Jason P. Lerch[1,4,5]*

* M.P. and J.L. contributed equally to this work.

Corresponding authors email ✉: clemence.ligneul@ndcn.ox.ac.uk

Affiliations

[1]Wellcome Centre for Integrative Neuroimaging, FMRIB, Nuffield Department of Clinical Neurosciences, University of Oxford; [2]Cardiff University Brain Research Imaging Centre (CUBRIC), School of Psychology, Cardiff University, Cardiff, UK; [3] School of Computer Science and Informatics, Cardiff University, Cardiff, UK; [4]Mouse Imaging Centre, The Hospital for Sick Children, Toronto, Ontario, Canada; [5]Department of Medical Biophysics, University of Toronto, Toronto, Ontario, Canada

Abstract

It is currently impossible to non-invasively assess cerebellar cell structure during early development. Here we propose a novel approach to non-invasively and longitudinally track cell-specific development using diffusion-weighted magnetic resonance spectroscopy in combination with microstructural modelling. Tracking metabolite diffusion allows us to probe cell-specific developmental trajectories in the cerebellum and thalamus of healthy rat neonates from post-natal day (P) 5 to P30. Additionally, by comparing different analytical and biophysical microstructural models we can follow the differential contribution of cell bodies and neurites during development. The thalamus serves as a control region to assess the sensitivity of our method to microstructural differences between the regions. We found significant differences between cerebellar and thalamic metabolites diffusion properties. For most metabolites, the signal attenuation is stronger in the thalamus, suggesting less restricted diffusion compared to the cerebellum. There is also a trend for lower signal attenuation and lower ADCs with increasing age, suggesting increasing restriction of metabolite diffusion. This is particularly striking for taurine in the thalamus. We use biophysical modelling to interpret these differences. We report a decreased sphere fraction (or an increased neurite fraction) with age for taurine and total creatine in the cerebellum, marking dendritic growth. Surprisingly, we also report a U-shape trend for segment length (the distance between two embranchments in a dendritic tree) in the cerebellum agreeing with age-matching morphometry of openly available 3D-Purkinje reconstructions. Results demonstrate that diffusion-weighted MRS probes early cerebellar neuronal development non-invasively.

Introduction

The cerebellum is a well-conserved structure across species and particularly across mammals. The cerebellar cortex is a highly folded structure organized in three layers: the molecular layer (containing the notable Purkinje cell dendritic trees), the Purkinje layer (containing the somas of Purkinje cells), and the granular layer (containing the granule cells). Projections to the deep cerebellar nuclei form the cerebellar white matter. Despite its small size (compared to the cerebrum), it contains more than half of the total brain neurons: this is mainly due to the granule cells, very small and densely packed cells, some of the smallest of the brain, presenting a very simple morphology[1]. On the other hand, the Purkinje cells are one of the largest types of neurons, and most complex cells in the brain. Cerebellar development is protracted[2], starting from birth (or the last trimester of pregnancy) to a few weeks old in rodents (or 2 y.o. in humans)[3]. The cerebellum is involved in many basic and high-level functions, from motor control to social skills, and it is known to be affected in a number of neurodevelopmental disorders[4].

During early development, neurons arborise. Their morphology becomes more complex and exhibits denser branching. In rodents, Purkinje cells' dendritic trees start growing at birth. In 30 days, they evolve from a simple soma (~10 µm diameter) to a large cell with a highly branched and planar dendritic tree (soma diameter ~20 µm, area ~10,000 μm^2 in the mouse[5]). Purkinje cell morphology can be altered in autism spectrum disorders (ASD), as shown post-mortem, in humans[6] and multiple mouse models of ASD. Specifically, they show an increased spine density in Tsc1 mutant mice[7], an overgrowth of the dendritic tree and abnormal branching in PTEN KO mice[8], a reduction of the dendritic tree in AUTS2 mice[9]; and general alterations in developmental disorders[10–13].

All cerebellar outputs transit via the deep cerebellar nuclei (DCN), and a couple of them project to the thalamus before spreading to the cortex. The thalamus is considered a relay station in the brain and contains about 60 nuclei on unique pathways. Some thalamic nuclei are involved in psychiatric disorders, and more specifically, the microstructure of the mediodorsal nucleus and the pulvinar nucleus are altered in schizophrenia and psychosis[14]. Some other nuclei are involved in neurodevelopmental disorders (e.g., the lateral reticular nuclei in ASD[15]). Generally, these disorders are associated with an altered thalamic connectivity[14]. Thalamocortical projections are crucial for the cytoarchitectural development of the cortex[16,17].

Neurodevelopmental disorders, or even psychiatric disorders with a neurodevelopmental origin such as schizophrenia[18], generally need better neurobiological characterisation during development[19].

Rodents reach adulthood after a couple of months and are an ideal model for mammal brain development. While brain cell developmental trajectories are key to assessing neurodevelopment, there is a lack of translational techniques allowing for a non-invasive measure of their properties. Typically, EEG and MEG signals contain brain activity cell-specific information. Still, it is hard to retrieve in practice, and the existing forward or inverse models notably use prior information on cell morphology. PET can be cell-specific and provide information about metabolism, but it is blind to cell morphology and relies on radioactive ligands, making it very expensive and potentially harmful. fNIRS and ultrasounds are too indirect to measure cell-specific information as they rely on the hemodynamic response. Last but not least, MRI is non-invasive and non-harmful. The MR signal can be sensitised to assess different tissue properties. In the following paragraphs, we will summarise the importance and limitations of some MR methods sensitive to brain structure and microstructure during development and introduce our primary method, namely diffusion-weighted MR spectroscopy (dMRS).

(***Structural MRI: anatomy***) Manganese-enhanced MRI (MEMRI) is particularly suited to studying whole-brain early development in rodents. It provides high structural contrast and a fast acquisition time in neonates[2,20]. Still, the method is blind to the microstructural changes that lead to the volumetric changes reported.

(***dMRI: microstructure***) Diffusion-weighted MRI (dMRI) measures the diffusion properties of water in the brain: restricted and hindered by cell membranes, water diffusion provides an indirect measure of the tissue microstructure[21]. dMRI is versatile and applied in numerous applications, including the characterisation of the microstructural organisation during neurodevelopment in rodents and, to a lesser extent, in humans. Comparison with postmortem microscopy shows a correlation between a high cortical fractional anisotropy (FA) at birth and the presence of radial glia. The latter progressively disappears in the first week along with an FA decrease, illustrating the potential of dMRI to characterise neurodevelopment[22,23]. In the cerebellum, the dense folding limits diffusion imaging to exploring white matter or ex vivo samples[24].

(***dMRS: cell-specific microstructure***) Water is ubiquitous and can only partially disentangle the contribution from different tissue compartments (e.g. intra and extracellular space). Diffusion-weighted magnetic resonance spectroscopy (dMRS) measures the diffusion properties of metabolites. Brain metabolites are mostly intracellular, with some more specific to neurons (e.g., N-acetyl-aspartate, NAA, and glutamate, Glu) and others more specific to glial cells (e.g., choline compounds, tCho, and myo-inositol, Ins), therefore different cellular compartments can be resolved[25]. However, metabolites are 10^4-fold less concentrated than water, requiring large measurement volumes for dMRS (typically ~ 50-100mm^3 in rodents), and long acquisition times. As for dMRI, some dMRS acquisition parameters, such as the diffusion weighting and diffusion time, enable the signal to be sensitised to different cellular morphological scales (e.g., cellular processes, cell bodies, cell extension). Using multiple diffusion times and a post-hoc model, cellular morphological parameters can be estimated from dMRS[26]. They correlate with neuronal and glial morphologies extracted from histological measures in the healthy, adult mouse[27,28]. More specifically, it has been shown that myo-inositol diffusion properties reflect astrocytic morphology in an induced model of astrocytic hypertrophy[29], and in a mouse model of demyelination where astrocytic activation was expected[30]. Choline compound's diffusion properties were associated with microglial activation in human disease[31], or in an LPS-induced brain inflammation model[32]. However, to our knowledge, very few studies have used dMRS to probe changes in neuronal morphology, and none have attempted to probe neuronal development in early life.

Here, we propose a non-invasive method to monitor cellular brain development. We focus on two regions with different developmental timelines: the cerebellum and the thalamus. As described above, the cerebellum expands greatly after birth, when the Purkinje cells dendritic trees start growing. This slow maturation exposes the cerebellum longer to developmental insults. In contrast to the cerebellum, the thalamus develops relatively quickly, and its neurons expand and complexify more rapidly[2,33] (**Figure 1A**).

By contrasting these two regions, we want to assess the sensitivity of the proposed method. We scanned developing rats from postnatal day five (P5) to P30. We first used MEMRI to confirm the protracted cerebellar development compared to the thalamus. We then acquired diffusion properties of metabolites to probe short- and long-range restriction (i.e., soma restriction and branching). To interpret our data, we applied two biophysical models (one analytical and one computational) to characterise the specific changes in microstructure. We expected monotonic changes in microstructural parameters in both regions, reflecting cell growth, with thalamic properties plateauing earlier than cerebellar properties. This is mostly what we report in our observations. However, we

report a U-shape trend for the cerebellar segment length ($L_{segment}$, the distance between two embranchments of a dendritic tree) that matches openly available 3D cell reconstructions. In contrast to common findings in the adult brain, we report that tNAA and Glu do not provide reliable morphological neuronal markers in neonates. We identify instead total creatine (tCr) and taurine (Tau) as more reliable markers for tracking early neuronal development. We believe that this is a promising method to track early neuronal development, particularly in the cerebellum, where microstructure changes drastically postnatally.

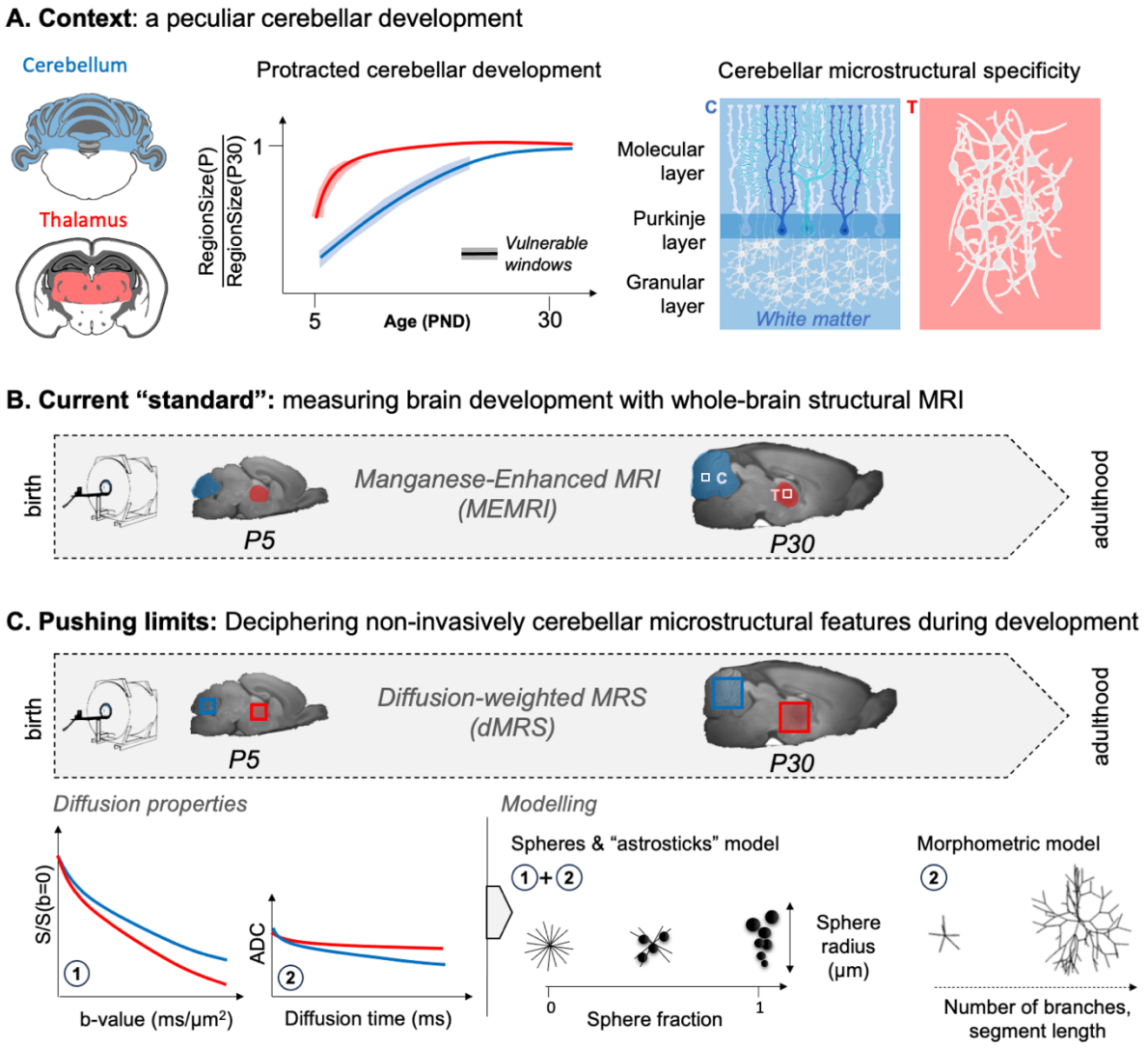

Figure 1: **Overview of the rationale of the study**. (A) Context: the cerebellum exhibits protracted growth compared to other brain regions (e.g., thalamus), making it a particularly vulnerable region for neurodevelopmental disorders. Its specific microstructural organisation (i.e. layered with Purkinje cells and granular cells) changes between birth and adulthood. (B) The current "standard" is to probe regional growth with manganese-enhanced MRI (MEMRI). However, it is not sensitive to the underlying microstructural changes. (C) Pushing limits: diffusion-weighted MRS (dMRS) can potentially assess cell-specific microstructural changes in given regions during development. Different measures of metabolites diffusion properties (apparent diffusion coefficient, ADC, at long diffusion times, signal attenuation, S, at high diffusion weighting, b-values) can be interpreted with biophysical modelling and help characterise the nature of the microstructural changes.

Results

Structural imaging confirms protracted cerebellar growth.

Representative slices from intra-age non-linear registration are shown in **Figure 2A**, underlying the cerebellar unfolding. Both cerebellar and thalamic volumes are just below 50µl at P5 (**Figure 2B**). However, the segmentation at P5 is poor, as explained in Methods (**Figure S1**), hence data at this time point should be treated cautiously, although the cerebellum and the thalamus, which are medial line structures, are less affected by the atlas distortions.

The cerebellum triples in volume, between P5 and P30, reaching 90% of its P30 volume at P20, while the thalamus reaches 90% of the P30 volume at P15.

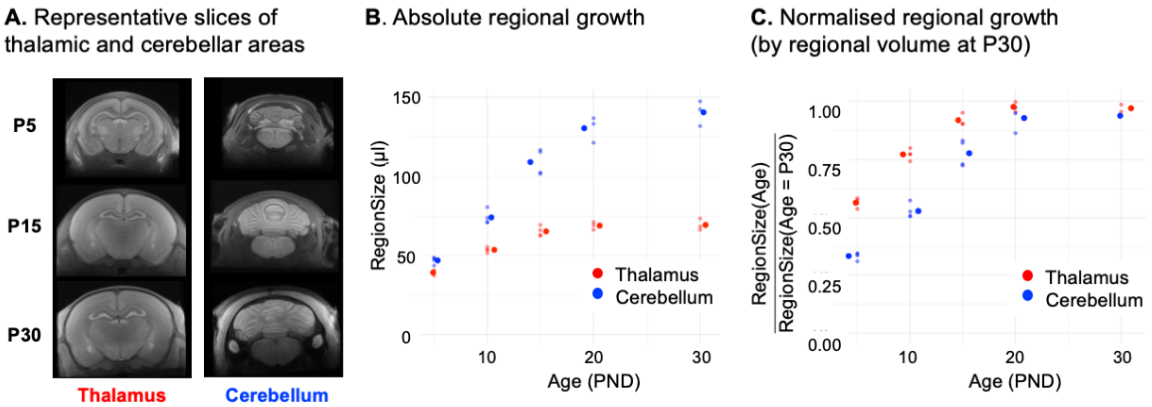

Figure 2: **Manganese-enhanced MRI confirms protracted cerebellar growth in rat pups.** (A) Representative slices around the thalamus and cerebellum of non-linearly averaged images acquired at P5, P15 and P30. (B) Absolute volumetric changes are shown for the segmented thalamus and cerebellum. Large dots correspond to the mean and small dots to individual data points. (C) Normalised volumetric changes. Volume at each age is normalised by the P30 volume. Large dots correspond to the mean and small dots to individual data points.

Metabolic profile changes with age.

The metabolic profile changes noticeably between P5 and P30 as shown in **Figure 3A**. The absolute concentrations of metabolites, estimated by LCModel using the b_0 averaged spectra, shown in **Figure 3A,** were normalised by the absolute concentration of macromolecules, MM (**Figure 3B**). Normalising by the MM content is an unusual choice. Conventionally, metabolite absolute concentrations are normalised by the water content in the voxel or by the tCr absolute concentration, which is considered stable in the healthy brain. However, this study compares regions with different relaxation properties at different ages, with different metabolites profiles in adulthood. The water relaxation properties are different between the thalamus and cerebellum, and both water relaxation properties and content change with age[34,35]. The tCr concentration changes substantially with age (about +50% in the cerebrum between P7 and P28) and is known to be higher in the cerebellum in adulthood (about +40-50% compared to the cerebrum)[35,36]. The MM concentration increases by about 30% between P7 and P28. MM resonances mainly come from the cytosolic proteins and although their content might slightly vary between regions in the healthy brain, they make a reasonable intracellular reference if SNR allows. We report normalisation by water in **Figure S2**, but the results are noisier than those normalised by MM. Between P5 and P30, metabolite/MM ratios increase for tNAA, Glu, Gln and Ins, and decrease for Tau, Gly, PE and tCho. Note that the increase in tNAA signal with age is protracted in the cerebellum compared to thalamus and has not reached a plateau at P30. These results generally match the metabolic concentrations measured with gold-standard classical MRS in the striatum, cortex and hippocampus of developing rats reported in Reference [35]. We observe that tCr/MM

increases strongly in the cerebellum between P5 and P30 but appears stable in the thalamus, while Reference [35] reported a 30% increase between P7 and P28 in the 3 ROIs. However, they also reported a 30% increase of the macromolecular content during this developmental period, matching our tCr/MM observation in the thalamus.

Metabolite diffusion properties differ between regions and change with age.

Thalamic (**Figure 4A**) and cerebellar (**Figure 4B**) signal attenuations up to b=30 ms/µm^2 and ADCs at TM=100-1000 ms are shown for tNAA, Glu, tCr, Tau, tCho and Ins. These diffusion properties differ between both regions at each age (see **Figure S3** for a region-to-region visual comparison). For most metabolites (except tCho), the signal attenuation is stronger in the thalamus, suggesting less restricted diffusion compared to the cerebellum. There is also a trend for lower signal attenuation and lower ADCs with increasing age for some metabolites, suggesting increasing restriction of metabolite diffusion. This is particularly striking for Tau in the thalamus. To give an estimation of the MRS fit performance, CRLBs are given for tNAA, Glu, tCr, Tau, tCho and Ins for the different diffusion conditions in Table S1.

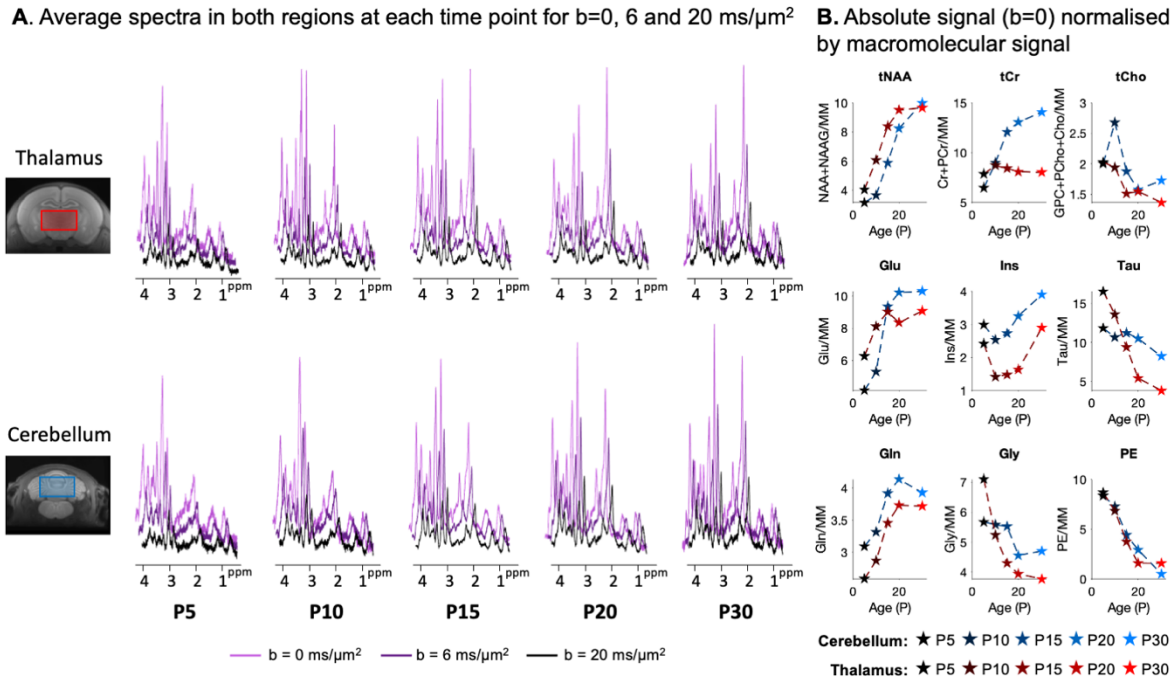

Figure 3: **Metabolic profile changes postnatally**. (A) Spectra were binned per time point, region and b-value and averaged after phase and frequency correction. The SNR is clearly lower at P5/P10 in both regions: the voxel is about half of the P30 voxel size, and more animals were outliers. The SNR is also lower at P30: the rat size was slightly too big for the mouse cryoprobe at this age, so the skull is not at the top of the probe and the sensitivity is suboptimal (B) Spectra at b=0.035 ms/µm^2 displayed in (A) were quantified with LCModel and absolute metabolite concentrations were normalised by the absolute macromolecular concentration and levelled to get Signal(tCr,P30)/Signal(MM,P30)=8 in the thalamus. **See Figure S2** for a comparison with normalisation by water and individual estimations (rather than average spectra quantification).

Biophysical modelling underlines different developmental trajectories of cell microstructure between the cerebellum and the thalamus.

Data were fitted with a spheres + "astrosticks" model and a morphometric model (more details in the Methods section). The spheres + "astrosticks" model captures diffusion within spheres (representing cell bodies) and randomly oriented sticks (representing cell processes/neurites): parameters extracted

are sphere fraction, f_{sphere} (or equivalently neurite fraction as 1-f_{sphere}) and cell radius, R. The parameter space (sphere radius vs sphere fraction) is represented in the 3rd column of **Figure 4A** (cerebellum) and **Figure 4B** (thalamus) for tNAA, Glu, tCr, Tau, tCho and Ins at all ages (see **Figure S4** for a region-to-region visual comparison).

Mean values and standard deviations are reported in **Table 1**, along with the results from the linear mixed effect model ~ Age + Region + Age:Region + (1|PupID). The fits on averaged data, for binned spectra by age and region, are shown in **Figure S5**.

The morphometric model, only applied to averaged ADCs at long t_d, interprets diffusion in branched structures: the segment length, $L_{segment}$ is reported on the last column of **Figure 4A/B** (see **Figure S6** for a region-to-region visual comparison and **Figure S7** for all parameters estimated by the morphometric model: D_{intra}, N_{Branch}, $L_{segment}$).

Neuronal markers: tNAA and Glu are primarily concentrated in neurons in adulthood.

- Thalamus: The sphere fraction and the radius estimated from tNAA and Glu diffusion properties do not change much with age. For both metabolites, f_{sphere} is around 0.25 and R decreases to 5-6 µm. $L_{segment}$ is stable with age for tNAA, but shows a reduction at P15-P20 for Glu.
- Cerebellum: The sphere fraction and the radius estimated from tNAA diffusion properties vary with age. f_{sphere} nears 0.5 in the cerebellum and R decreases below 5 µm for tNAA and Glu. $L_{segment}$ decreases until P15 for both tNAA and Glu.

Between regions, sphere fraction differs significantly (**Table 1**).

Glial markers: tCho and Ins are primarily concentrated in glial cells in adulthood. The general trend is a high sphere fraction (~0.7-0.9) for Ins and moderately high (~0.5-0.6) for tCho. The radius estimated from tCho differs significantly between regions. Note the trend of decreasing sphere fraction in the cerebellum with age. Data at P15 for Ins in the thalamus were individually not reliable enough to apply the spheres + astrosticks model (c.f. Table S1 and the particularly higher CRLBs at P15 for Ins).

Non-specific markers: tCr and Tau are not known to be compartmentalised in a specific cell-type.

- Thalamus: Parameter estimates for tCr diffusion properties do not change substantially with age (f_{sphere}~0.35, R~6.5µm). Tau parameters estimation varies a lot with age: R shows a substantial decrease and f_{sphere} increases.
- Cerebellum: f_{sphere} decreases from 0.63 (P10) to 0.41 (P30) for tCr, but R is stable. Tau follows a similar pattern, although with an overall lower f_{sphere} (0.43 at P10 to 0.29 at P30). $L_{segment}$ increases in the cerebellum from P10 for tCr and increases P15 for Tau.

Between regions, the sphere fraction differs significantly for both metabolites (**Table 1**), but only Tau exhibits a significant change with age, and this change is different between regions (significant interaction term). For Tau, the radius is significantly different between regions, changes significantly with age and this change is different between regions (significant interaction term).

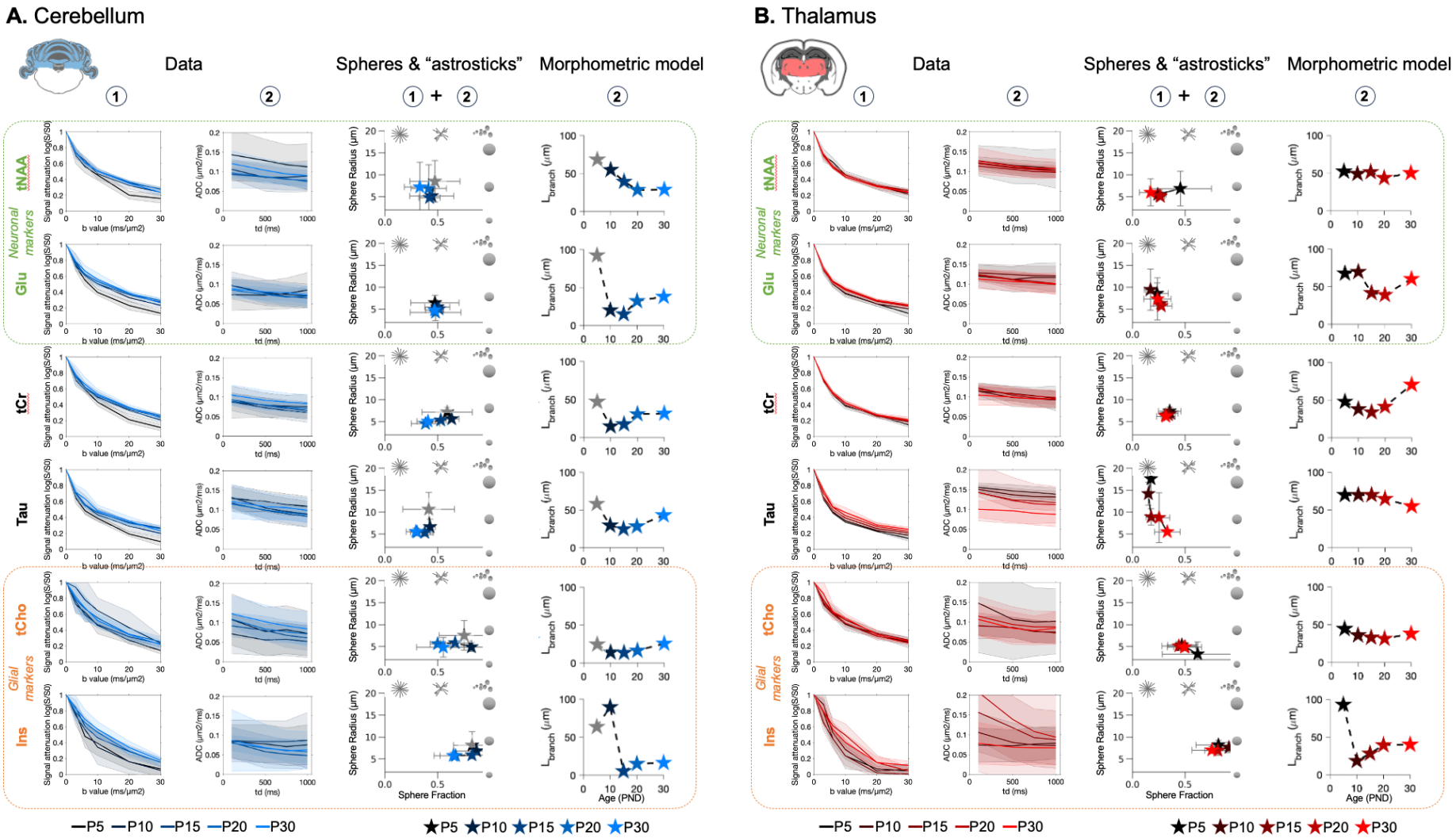

Figure 4: Biophysical modelling issued from metabolites diffusion properties shows differential developmental trajectories in the cerebellum (A) and in the thalamus (B). The first column (A,B) reports the signal attenuation as a function of b-value at TM=100ms, and the second column reports the ADC varying with diffusion time. Shadowed error bars represent the standard deviations. Modeling results from the spheres+"astrosticks" model is reported in the third column (A,B). P5 is shaded in the cerebellum due to possible motion artefact. The parameter space (sphere fraction, sphere radius) is displayed. Error bars represent the standard deviations. L_{length}, modeling output from the morphometric model is shown in the fourth column (A,B). P5 is shaded in the cerebellum due to possible motion artefact.

Table 1: Mean values and standard deviations for parameters extracted from the spheres + "astrosticks" model (sphere radius and sphere fraction). Statistics come from a linear model accounting for age and region as fixed effect. The interaction term was included only if it improved the fit significantly (c.f. Methods). p-values highlighted in yellow pass the α=0.05 threshold after multiple comparison correction and green p-values pass the α=0.01 threshold (Bonferroni correction, 12 hypotheses).

	CEREBELLUM					**THALAMUS**					(Radius, Fraction) ~ Region*Age + (1|PupID) *p-values before multiple comparison correction*		
Age (PND)	5	10	15	20	30	5	10	15	20	30	Region	Age	Region:Age
	NAA+NAAG					NAA+NAAG							
Radius (µm)	8.51	5.18	4.78	6.92	7.21	6.84	5.52	5.05	5.24	5.97	3.69E-01	7.13E-01	
std(Radius) (µm)	4.72	1.10	0.58	5.34	5.66	3.96	0.77	0.59	0.55	3.08			
f_{sphere}	0.47	0.45	0.42	0.42	0.33	0.46	0.24	0.27	0.26	0.17	1.20E-04	9.11E-04	
std(f_{sphere})	0.24	0.21	0.10	0.17	0.15	0.30	0.08	0.04	0.03	0.11			
	Glu					Glu							
Radius (µm)	6.59	5.49	5.04	4.26	4.79	8.57	9.46	6.26	5.71	7.32	1.14E-03	1.74E-02	
std(Radius) (µm)	1.78	0.91	0.24	1.88	0.12	2.42	4.70	0.62	0.62	4.82			
f_{sphere}	0.47	0.50	0.51	0.48	0.47	0.23	0.17	0.27	0.28	0.24	2.27E-06	7.45E-01	
std(f_{sphere})	0.24	0.12	0.04	0.24	0.09	0.11	0.06	0.07	0.10	0.13			
	Cr+PCr					Cr+PCr							
Radius (µm)	7.17	5.61	5.31	4.54	5.07	7.38	6.87	6.53	6.45	6.18	1.49E-01	1.83E-03	5.13E-02
std(Radius) (µm)	1.09	0.58	0.32	0.78	0.50	0.92	0.57	0.31	0.69	0.67			
f_{sphere}	0.59	0.63	0.53	0.39	0.41	0.35	0.36	0.34	0.31	0.32	1.32E-07	3.26E-01	6.55E-03
std(f_{sphere})	0.24	0.07	0.05	0.14	0.10	0.11	0.07	0.02	0.04	0.09			
	Tau					Tau							
Radius (µm)	10.63	6.63	5.32	5.41	5.56	17.57	14.18	8.90	8.73	5.50	4.27E-08	3.53E-12	7.41E-04
std(Radius) (µm)	3.83	1.76	0.83	0.83	0.85	2.97	2.58	1.88	5.67	0.57			
f_{sphere}	0.42	0.43	0.38	0.31	0.29	0.18	0.15	0.18	0.25	0.33	2.51E-10	2.82E-04	8.66E-06
std(f_{sphere})	0.25	0.05	0.08	0.06	0.09	0.03	0.03	0.05	0.10	0.12			
	tCho					tCho							
Radius (µm)	7.83	4.88	5.83	5.59	4.83	3.28	5.35	4.91	5.10	4.86	5.81E-04	2.05E-01	9.54E-03
std(Radius) (µm)	3.48	1.03	0.53	0.58	2.24	2.77	0.59	0.56	1.07	0.87			
f_{sphere}	0.80	0.82	0.67	0.50	0.55	0.62	0.47	0.50	0.44	0.50	4.20E-04	5.18E-03	
std(f_{sphere})	0.19	0.20	0.14	0.07	0.25	0.34	0.13	0.11	0.16	0.16			
	Ins					Ins							
Radius (µm)	8.80	6.81	5.89	5.74	5.75	8.18	7.60		6.93	7.00	2.19E-03	2.11E-03	
std(Radius) (µm)	3.11	0.56	0.51	0.60	0.75	1.05	1.16		1.14	0.79			
f_{sphere}	0.83	0.87	0.83	0.67	0.65	0.82	0.92		0.81	0.76	2.28E-01	1.44E-02	
std(f_{sphere})	0.20	0.22	0.15	0.15	0.18	0.21	0.14		0.13	0.19			

Discussion

As in Reference [2] we used MEMRI to validate the protracted development of the cerebellum in rat neonates[3], unfolding and tripling volume between P5 and P30. Early developmental cell-specific cerebellar and thalamic microstructural features were assessed with dMRS.

We specifically report diffusion properties for neuronal markers tNAA and Glu, glial markers tCho and Ins, and the non-specific markers tCr and Tau. Metabolites exhibit significantly different diffusion properties between regions, demonstrating the relevance of dMRS to probing early cell structure development. f_{sphere} is notably higher in the cerebellum for metabolites compartmentalised fully (tNAA, Glu) or partially (tCr, Tau) in neurons, suggesting the influence of the cell-body dense granular layer of the cerebellum. f_{sphere} possibly reflects the relative volume of sphere-like structures (e.g., cell bodies) compared to the relative volume of fibrous structures (e.g., cell processes, fibres).

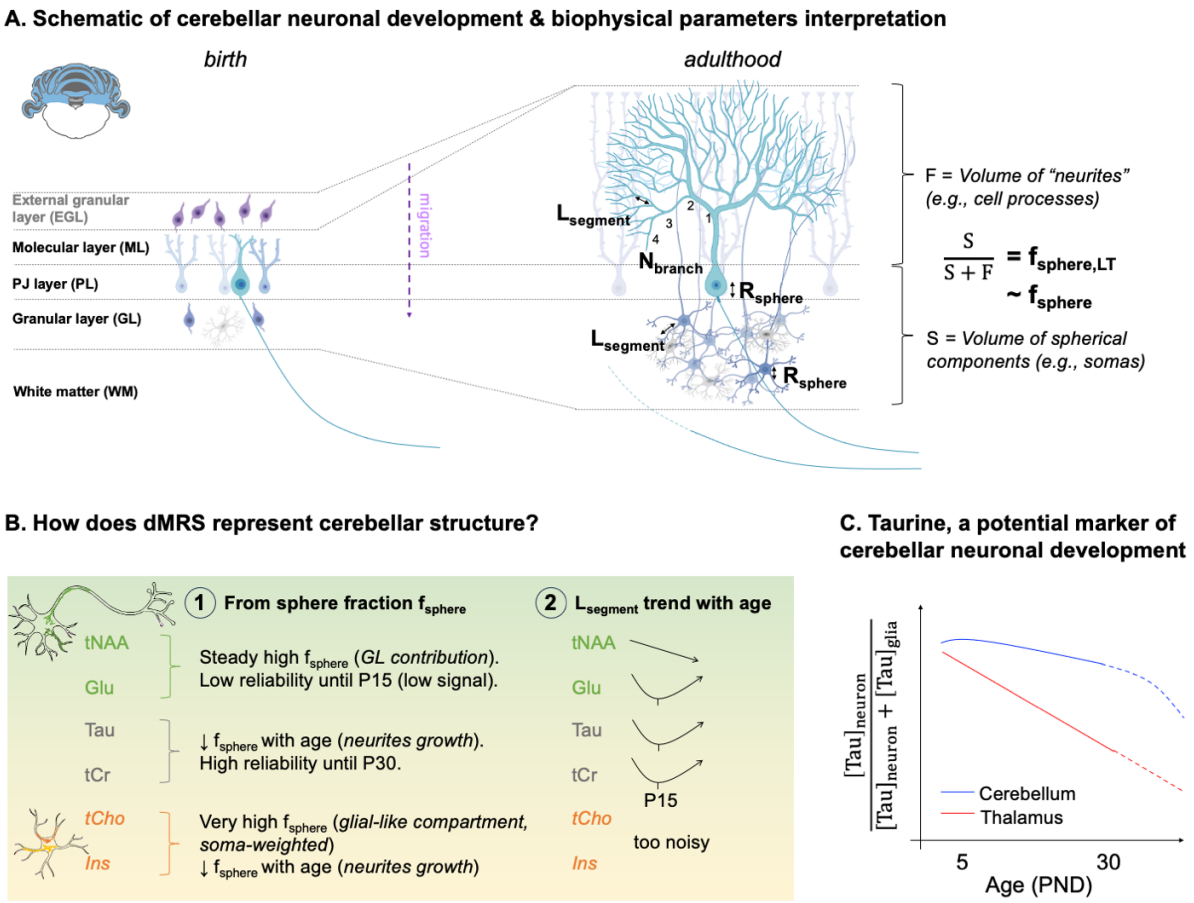

Figure 5: **The biophysical parameters are interpreted based on the cerebellar microstructural development and main results are summarised**. Italic font corresponds to possible interpretations. (A) Schematic of cerebellar neuronal development and biophysical modelling parameters interpretation. $L_{segment}$ is interpreted as the distance between two branches of the dendritic tree, N_{Branch} as the number of embranchments. The sphere radius R_{sphere} is interpreted as the average soma radius (i.e. granule and Purkinje cells). $f_{sphere,LT}$ represents the ratio of cerebellar layer thicknesses between the layers rich in sphere-like cell components (e.g., somas in the I/EGL, GL and PL) and the layers rich in fibrous cell components (e.g., cell processes or "neurite" in the ML). $f_{sphere,LT}$ can be seen as a rough approximation of f_{sphere} and is inversely related to the dendritic tree growth, see Table S2. (B) Summary of the cerebellar results coming from the modelling. (1) and (2) refer to the models depicted in Figure 1. (C) Tau seems to change compartments in the thalamus with age, going from neuronal-like compartments (low sphere fraction) to glial-like compartments (high sphere fraction), also indicated by its important signal drop with age. It suggests that Tau is a marker of neuronal maturation. Its concentration

remains high up to P30 in the cerebellum. Tau properties in the cerebellum (decreasing sphere fraction + relatively low sphere fractions) and contrast with the thalamus suggest that Tau could be a marker of cerebellar neuronal development.

A study of human WM using diffusion MRI reported an increase in FA and a decrease in MD with age in early life.[22] In mice, the same relationship was found in both WM and GM[37]. We report similar dMRI trends, in both cerebellum and thalamus (**Figure S8**).

We also report dMRS changes with age in both regions. The general trend we find for lower signal attenuation and ADC decrease (for some metabolites) with increasing age aligns with these reported dMRI observations, and could reflect overall microstructural complexification. However, the different nature of the signal (metabolites: mostly intracellular and low compartmental exchange vs. water: ubiquitous and fast exchange) prevents close co-interpretation.

f_{sphere}(tCr, Tau) decreases with age in the cerebellum, meaning that tCr and Tau are located in compartments where the relative contribution of sphere-like structures (e.g. cell-bodies) decreases. In other words, it reflects cerebellar cell growth and complexification (**Figure 4A, Figure 5A**). In the cerebellum, while soma morphologic maturation mostly happens in the first week[38], Purkinje cell dendritic expansion is rapid before P15 but then continues to mature up to the end of the 4th week[38,39]. Tau diffusion properties might reflect the development of Purkinje cells: (i) in cats, which cannot synthesise Tau and must source it from their diet, Tau dietary deficiency delays cortical and cerebellar maturation[43], meaning that Tau is also crucial in early development, and (ii) in the cerebellum, immunohistochemistry studies locate Tau in adult Purkinje cells[40–42]. These observations align well too with the high Tau levels we still detect in the cerebellum at P30 (**Figure 3B**).

The diffusion properties of glial metabolites, f_{sphere}(Ins) and f_{sphere}(tCho), also tend to decrease with age. This could be explained by another cerebellar peculiarity: Bergmann glia develop long processes along Purkinje cells and this specific growth could contribute to the f_{sphere}(tCr,Tau) decrease.

Validation would require an atlas of all types of cerebellar cellular processes and bodies with estimates of their relative contribution. Such a resource would be immensely valuable but does not exist. Using literature data, we use the relative thicknesses of the EGL, IGL, PL ("cell body-like" layers) and ML ("fibre-like" layer) to derive $f_{sphere,LT}$, a proxy of f_{sphere}, as illustrated in **Figure 5A** and reported in Table S2 and **Figure S11**. $f_{sphere,LT}$ represents the contribution of sphere-rich layers compared to fibre-rich layers. The evolution of $f_{sphere,LT}$ trend with age is comparable to f_{sphere}(tCr). Although f_{sphere}(tCr) and f_{sphere}(Tau) have similar trends, f_{sphere}(Tau) values are overall lower, and below $f_{sphere,LT}$ values (**Figure S11**). This lends weight to the idea that Tau is preferentially located in cerebellar neurons during cerebellar development (and potentially less so in granule cells). In comparison, tCr, which appears more evenly spread between all cerebellar cell types, tracks the evolution of $f_{sphere,LT}$ more closely. Note that Tau has a higher D_{intra}[44] compared to the other metabolites, potentially affecting the parameter estimation given for Tau. As described in Methods, the fit for Tau was substantially improved for D_{intra} > 0.6 μm^2/ms. The results for D_{intra}=0.7 μm^2/ms are similar for all the other metabolites (**Figure S9**), and generally improved the estimated sphere radius standard deviation. Additionally, the evolution with age of (R,f_{sphere}) is then very similar for tNAA and Tau, reinforcing the idea that Tau is neuronal in the cerebellum.

In the thalamus, the decrease in Tau content (**Figure 3B**) and the change in Tau diffusion properties (**Figure 4B**) point towards a change of compartmentation with age. Contrary to the trend in the cerebellum, f_{sphere}(Tau) consistently increases with age in the thalamus (**Figure S9**). This means that Tau diffuses in a space with fewer and fewer processes during development, which is incompatible with the hypothesis that Tau stays in the same compartment. Neurons, but also microglia[45] or

astrocytes[46–48] develop with increasing ramification. Neurons are already branched at P10 in the thalamus[33] (shown by a low f_{sphere}(tNAA, Glu) at P10). f_{sphere}(Tau) at P10 nears f_{sphere}(tNAA, Glu), indicating that Tau might be located in neuronal compartments in the neonatal thalamus. Although this hypothesis is not verifiable in existing literature, some in vitro studies show that Tau contributes to neuronal proliferation[49] and neuronal growth[50]. At P30, f_{sphere}(Tau) is closer to f_{sphere}(tCho,Ins), indicating that Tau might be located in glial compartments in adulthood. Indeed, immunohistochemistry studies locate Tau in adult thalamic glia[42].

We suggest Tau as a cerebellar marker of early neuronal development, possibly more specifically of Purkinje cells. We confirm in this study the observation from Reference [35] that both tCr and Tau have high spectroscopic signals in neonates. They are the two metabolites most reliably quantified up to P15 in both regions (continuing for Tau in the cerebellum up to P30), and the estimates of their diffusion properties are the most confident, contrary to the usual neuronal markers, tNAA and Glu. tCr stands as a good marker, too. However, there is no indication of a preferential neuronal compartmentation for this metabolite during early development, hence it is less specific to neurons, and probably even less to Purkinje cells. Because Tau seems to switch compartments in the thalamus between birth and adulthood, we do not think its diffusion properties reliably inform thalamic neuronal morphological development. In both human[51,52] and rhesus monkey[53] brains, Tau content increases at birth and then decreases with age, and is therefore a marker of the immature brain in both species. Although Tau concentration is low in the adult human brain, it is more concentrated in the cerebellum in adulthood[52,54]. A similar finding was made in the adult rhesus monkey brain[53], indicating a conserved pattern across species of Tau properties in the cerebellum. These observations form a good basis for translation. Although dMRS in infants has substantial challenges, they are worth trying to overcome for a putative cerebellar marker of early neuronal development which could help understand neurodevelopmental disorders [3].

We also observed a protracted increase in tNAA signal in the cerebellum compared to the thalamus. tNAA is usually described as a neuronal osmolyte, meaning it could reflect neuronal growth and maturation and be a marker of neuronal development. However, at the voxel level, its signal reflects the neuronal volumetric contribution, i.e. differences in neuronal densities might mask the effect of development. In contrast, we want to reiterate that dMRS is a normalised measure and dMRS outcomes are not affected by the neuronal density: they represent the average morphological properties of the cell types the metabolite belongs to.

We chose to interpret the dMRS data with two biophysical models: an analytical spheres & “astrosticks” model and a computational morphometric model. The analytical model was applied simultaneously to the signal attenuation at high b-values and the ADCs at long diffusion times, and on individual animals. In addition to the valuable biophysical biomarkers, it provides a good signal representation to evaluate the significance of the differences between diffusion properties of individual datasets. The experimental design was not suitable for a randomly oriented infinite cylinders (“astrocylinders”) model as in previous studies[28,29]. The mixing time used for the acquisition of signal decay at high b-values (TM=100 ms) is too long to enable sensitivity to fibre radius[26], hence the choice of “astrosticks” model. The sphere compartment was added to account for the high sphere fraction in the cerebellum, and for the nature of the neonatal brain (under-developed neurons). The RMSEs from the different models tested (**Figure S3**) tend to be more similar at P30, suggesting that it is less important to add a sphere compartment for modelling metabolites diffusion in the adult brain.

The computational morphometric model was applied to attempt to extract cell extension-related parameters, but the study design and data quality are suboptimal, and we could only reliably extract $L_{segment}$ and D_{intra} (**Figure S7**). D_{intra} is mostly stable with age in both regions. However, it sometimes drops or peaks, likely affecting the other parameters’ estimations. The longest mixing time (TM=1000

ms) is short compared to previous studies using a similar modelling approach[27,29], meaning that the diffusion path is shorter (i.e., about 30µm in this study compared to about 45µm in previous studies, assuming D_{intra}=0.5 µm^2/ms). Note that the higher D_{intra} of Tau is therefore an asset for probing early neuronal cerebellar growth. In our study, the number of embranchments (N_{branch}) was very poorly evaluated because of the high level of noise in the data. However, even with a better dataset quality and a more optimal study design, it is unlikely that the N_{branch} estimation could reflect the Purkinje cell morphometry because of their size and complexity in adulthood. If we had robust DTI in all animals (**Figure S8**), we would have included the fibre dispersion in the modelling (notably for the cerebellum), as in Reference [29]. However, since we acquired enough directions for the dMRS data to be powder-averaged, we expect that the WM contribution in the cerebellum is mostly reflected by a slight f_{sphere} drop, as exemplified by the $f_{sphere,LT}$ drop when including WM (Table S2).

Finally, we expected that $L_{segment}$ estimated from the morphometric model in the cerebellum would increase regularly with age, matching the dendritic tree development. For neuronal, or partly neuronal metabolites, we report an $L_{segment}$ decrease first. Except for tNAA, which consistently decreases in the cerebellum with age, $L_{segment}$ decreases until P15 for tCr, Tau and Glu and then increases, forming a U-shape curve. To better understand these results, we extracted the morphometries of developing Purkinje cells and developing thalamic interneurons (both in the mouse) from NeuroMorph.org. Interestingly, from these 3D reconstructed cells, we observe a decrease in $L_{segment,\ 3D\text{-}recon}$ up to P13 for Purkinje cells, whilst being quite stable in the thalamus (**Figure 6**), matching our non-invasive measurement trend. This could reflect the complexification of the dendritic tree following its expansion.

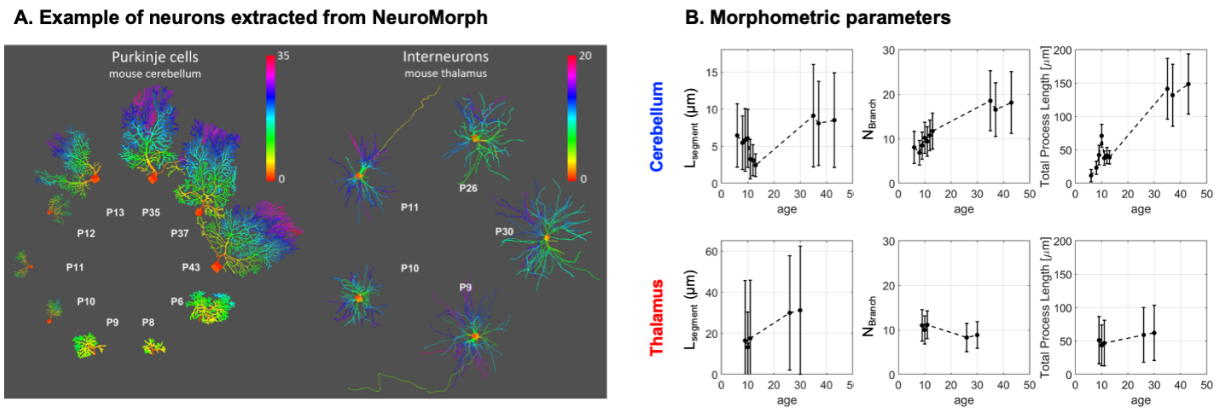

Figure 6: Morphometric parameters extracted from mouse real cells 3D reconstructions on NeuroMorph shows a decrease of $L_{segment}$ up to P13 in developing cerebellar Purkinje cells, but not in developing thalamic interneurons. (A) Examples of cells extracted from NeuroMorph. The total number of cells used per age and region is given in Supplementary Material. References: Cerebellum P6-P10[55], P10-P13[56], P35-P43[57]; Thalamus P9-P30[58] (B) The values of Branch Length (Lsegment), Branching Order and total process length are directly estimated from the morphology using the function stat_tree in the Trees Matlab Toolbox.

Conclusion

This study proposes diffusion-weighted MRS as a method to longitudinally and non-invasively measure cell-specific cerebellar and thalamic microstructural features during early development in rat neonates. We demonstrate the sensitivity of Taurine to early neuronal cerebellar development. This is a stepping-stone enabling further studies in pathological conditions.

Methods

Animals

Experiments were approved by the United Kingdom Home Office. 18 Sprague-Dawley rats (9 females) were scanned at P5, P10, P15, P20 and P30. Pups came from 3 litters (6 pups scanned per litter). Animals were induced with 4% isoflurane in oxygen and anaesthesia was maintained with 1-2% isoflurane in oxygen. Respiration was monitored with a breathing pillow. Temperature was monitored with a rectal probe, which was used as a cutaneous probe from P5 to P20 to avoid any risk of harm. Isoflurane level was adapted to keep the animals at 50-70 rpm and a warm water-circulation heating pad was used to keep the animals at 36-37˚C during scanning. Pups were gently held with foam and protected tape to minimise motion, because the neonatal skull is not suitable for the use of ear bars.

For logistic reasons we could not acquire MEMRI for all litters. Animals from the second litter had manganese-enhanced anatomical scans. To this end, they were intraperitoneally injected with a 50 mg/kg solution of $MnCl_2$ 24 hours prior to the scan. Under the age of P10, the dam received the intraperitoneal injection, and the manganese was transferred to the neonates via the maternal milk[2].

MRI acquisitions

Data were acquired on a 7T Biospec Bruker MRI scanner (Paravision 360.1, max gradient strength: 660 mT/m), equipped with a mouse quadrature cryoprobe, well-suited for rat neonates. An anatomical scan around the region of interest (thalamus or cerebellum) to place the voxel (T2-weighted, 2D RARE, R=8, 0.2 mm isotropic resolution, TE=33 ms, TR=3500 ms). For 6 animals, this scan was replaced by a whole brain manganese-enhanced anatomical scan (T1-weighted, 3D MGE, TE=2.4 s, TR=62 ms, 0.15 mm isotropic resolution).

Table 2: dMRS acquisition parameters.

dMRS Acquisition parameters					
Mixing time (ms)	**100**		**500**	**750**	**1000**
Diffusion time (ms)	104.25		504.25	754.25	1004.25
b-values (ms/µm^2)	0.035, 3.035, 6, 10, 20, 30		0.17, 3.17	0.26, 3.26	0.35, 3.35
TR (ms)	2000		2500	2750	3000
Total acquisition time	19min		5min	9min	19min
Repetitions	16x(4, 4, 6, 6, 8, 8)		16x(8,8)	16x(10,10)	16x(12,12)
Directions	16				
TE	34 ms (14 ms STE + 20 ms LASER)				
Voxel size					
Age	P5	P10	P15	P20	P30
Volume (µl)	22.05	29.95	48.75	54.60	54.60

dMRS acquisitions

A STELASER[59] sequence (TE=34 ms, diffusion gradient duration, δ=5 ms) was used for dMRS acquisitions. The voxel was placed in the cerebellum for 9 pups, and in the thalamus for the other 9

pups. Voxel size was increased with age to follow brain growth. Diffusion-weighted spectra were acquired at 4 mixing times (TM) and 2 b-values (c.f. Table 2 for detailed parameters): a small "b_0" used as a crusher for the stimulated echo, and b_0+3 ms/µm^2. Higher b-values were also acquired at the shortest diffusion time to probe restriction within cell bodies and enable inference of cell fraction and radius. The macromolecular baseline was acquired in the adult rodent with the same STELASER parameters (TE and δ), at the shortest TM=100 ms, but the stimulated echo was preceded by a double-inversion recovery (TI_1=2000 ms, TI_2=710 ms). The b-value was set to 10 ms/µm^2 to reduce the residual contribution of bulk metabolites, and the tCr peak residual at 4ppm (due to the shorter T_1) was corrected by subtracting a Lorentzian.

Processing

dMRS

Processing was achieved with a custom Matlab (The Mathworks) routine (https://github.com/clemoune/dmrs-neonates/tree/main/A_dMRS_processing):

- Signals from different coils were combined, using the water signal at the lowest b-value and shortest diffusion time.
- Outliers were identified and discarded, as described in[60].
    - For each transient i, the mean absolute upfield signal (range 1.9-4.5 ppm), $M_{up}(i)$ was computed.
    - Transients affected by motion are characterised by a clear drop of $M_{up}(i)$. Transients falling below the median(M_{up}) - 3xMAD threshold were discarded.
    - Experiments at high b-values are more susceptible to changing gradient direction (particularly if the voxel contains white matter tracts). To predict its effect across b-values and overcome the small number of acquisitions per unique condition (i.e. a (b-value, direction) pair), a diffusion kurtosis tensor was computed based on M_{up}. The MAD calculated at b=0 was used as a "ground truth" MAD and was reported to higher b-values (per direction). High b-values acquisitions are more easily corrupted by motion and therefore present an artificially high MAD.
- Individual transients were corrected for phase and frequency drifts and averaged across all diffusion directions (powder-averaged) via an arithmetic mean. In general, metabolites signal was visually detectable on single transients (with a line-broadening of 5 Hz), except at b=20,30 ms/µm^2 at P5, rendering these acquisitions more susceptible to motion artefacts.
- Any water residual was removed using a singular value decomposition method centred around the water region. If the baseline was heavily distorted despite this step due to very poor water suppression, the acquisition was discarded from the analysis.

Spectra were subsequently fitted with LCModel. The simulated basis set contained the following metabolites: Ace, Ala, Asp, Cr, GABA, Gln, Glu, Gly, GPC, GSH, Ins, sIns, Lac, NAA, NAAG, PCho, PCr, Tau, PE, and included a macromolecules (MM) baseline acquired experimentally (double-inversion recovery and b=10 ms/µm^2).

Diffusion properties of NAA+NAAG (tNAA), Glu, Cr+PCr (tCr), Tau, GPC+PCho (tCho) and Ins are reported. In order to model both signal compartmentalisation and restricted diffusion by cell membranes, we investigated metabolites diffusion through two sets of measurements: i) the direction-averaged signal decay as a function of the diffusion weighting b, keeping the diffusion time constant at 104.25 ms (time between diffusion gradients Δ fixed at 105.91 ms and δ fixed at 5 ms) and varying the strength of the diffusion-sensitizing gradients; and ii) the apparent diffusion coefficient

(ADC) as a function of increasing diffusion time (keeping δ fixed at 5 ms). For the measurements i), data are reported as the ratio S(b)/S(b=0). For the measurements ii), ADCs diffusion time dependencies are reported. ADCs are calculated following $ADC = \frac{-1}{b-b_0}\log\frac{S(b)}{S(b_0)}$. Negative ADCs were systematically removed as they point to a quantification error.

In the cerebellum, metabolites' signal attenuation at P5 is always much stronger and quite far off the other time points. The macromolecules' signal attenuation at high b-values is supposed to remain low[59] and can be used as an internal probe for motion artefact[44]. However, the macromolecules' signal attenuation is quite strong at P5 in the cerebellum (**Figure S8**), pointing out to a residual motion artefact despite careful processing. The spectroscopic signal in individual transients was too low at high b-values, notably in the cerebellum: it is possible that the spectral realignment failed.

MEMRI

The three first echoes of each MGE acquisition were averaged and denoised using the DenoiseImage function from the MINC toolbox, based on[61]. For each time point, an image with no obvious artefact and a good visual CNR was taken as the initial model and transformed into the Fischer atlas[62] space. Images were then processed using registration_tamarack.py with the MAGeT segmentation in the available Pydpider pipelines[63]. Due to the large deformations between P30 and P5, the P30 timepoint could not be used as a reference. An adequate atlas from P15 was generated in a couple of iterations (using a P20 atlas as intermediary). It was then used as a reference atlas and reference timepoint for the pipeline. The olfactory bulb and the more frontal parts were poorly registered because the image often had an intensity drop there, but it did not affect the registration of caudal regions, such as the cerebellum and the thalamus. Image with strong intensity differences, or corrupted by motion were removed from the analysis. The registration did not work well at P5, even when attempting to use an atlas generated at P10 (that is already slightly distorted).

Analysis

Signal decays at high-b values (at TM=100 ms) and ADCs at varying diffusion times were fitted together with a spheres and "astrosticks" (corresponding to randomly oriented sticks) model using the functions implemented in DIVE (https://git.fmrib.ox.ac.uk/fsl/DIVE). The DIVE toolbox uses the Gaussian phase distribution approximation We fitted the signal to:

$$\frac{S}{S_0} = f_{sphere} * S_{sphere}\left(D_{intra}, R_{sphere}|b_{value}, t_d, d\right) + (1 - f_{sphere}) * S_{sticks}(D_{intra}|b_{value})$$

Free parameters were R (sphere radius) and f_{sphere} (sphere fraction). D_{intra} (i.e. the metabolite intracellular free diffusivity) was fixed for both compartments at 0.5 μm^2/ms. Previous studies measuring brain metabolites diffusion properties at ultra-short diffusion-times[44,64] estimated the intracellular free diffusivity at 0.5-0.6 μm^2/ms for most metabolites (except Tau). However other studies using different (less direct) approaches reported lower D_{intra}[27,28], hence we tested a range of reasonable D_{intra}. D_{intra} was fixed 0.3, 0.4, 0.5, 0.6, 0.7 and 0.8 μm^2/ms. RMSEs between model fit and data were equivalent for all D_{intra}, except for Tau in the thalamus where increasing D_{intra} improved the fit, particularly until D_{intra}=0.5μm^2/ms. Moreover, parameters estimation was unrealistic for low D_{intra}. Increasing D_{intra} between 0.5 μm^2/ms and 0.7 μm^2/ms did not change the trend of the results, except for Tau in the thalamus (see **Figure S0** and Discussion). The fit was made robust to missing data (when excluded during processing).

To test for the model accounting best for our data, we tested different analytical models. RMSE between model fit and data were calculated for "astrosticks" only (1 free parameter, D_{intra}), "astrocylinders" (corresponding to randomly oriented infinite cylinders, 2 free parameters: D_{intra} and cylinder radius), spheres and astrosticks without constraint (3 free parameters) and spheres and astrosticks with D_{intra} fixed at 0.5 $\mu m^2/ms$ (**Figure S0**). RMSE were the lowest for spheres and astrosticks, and were very similar with and without the D_{intra} constraint. Hence the model with the least free parameters was chosen. Moreover, the results from the constrained spheres and astrosticks model were more stable and physically meaningful with the constraint on D_{intra}. The code used for the analysis can be found on: https://github.com/clemoune/dmrs-neonates/tree/main/B_Astrosticks_Spheres_model.

Long diffusion times:

Average ADCs at varying diffusion times were fitted with the morphometric model introduced in[27]. Modeling was performed using the dictionary generated for[29] with TM = 100, 750 ms predicted by interpolation, and a random forest regressor ('treeBagger' function in MatlabR2020b, with tree depth = 20; number of trees = 200 and other model hyper-parameters as per default) trained in a fully supervised fashion, using the ADCs time dependencies as input and the ground truth morphological parameters as targets; as loss function the mean squared error between predicted and ground truth parameters values was used. Parameters fitted were D_{intra}, N_{branch}, $L_{segment}$, SDN_{branch} and $SDL_{segment}$. Boundaries for fitting the model to data were respectively [0.1, 1], [2, 25], [5, 100], [2, 3] and [5, 10]. Given the data noise, only $L_{segment}$ and D_{intra} are estimated robustly. Fits for all parameters are shown in Supplementary Information.

Statistical analyses

Statistical analyses were run with R, using the "lmerTest[65] package. To assess whether diffusion properties were significantly different in the 2 regions during development, we applied a linear mixed effect model to the parameters extracted from the spheres + "astrosticks" model (sphere fraction and sphere radius), using age and region as fixed effects, and a random intercept for pups ID. An analysis of variance enabled to identify whether the inclusion of an interaction term age*region was necessary or not. Results were corrected for multiple hypotheses testing with a Bonferroni correction (6 metabolites,2 parameters = 12 hypotheses). The threshold corrected p-value is $4.2e^{-3}$ for α=0.05 and $8.3e^{-4}$ for α=0.01.

Funding

This work was funded by Wellcome. The Wellcome Centre for Integrative Neuroimaging is supported by core funding from the Wellcome Trust (203139/Z/16/Z and 203139/A/16/Z). For the purpose of Open Access, the corresponding author has applied a CC BY public copyright licence to any Author Accepted Manuscript version arising from this submission. MP is supported by UKRI Future Leaders Fellowship (MR/T020296/2).

REFERENCES

1. Haines DE, Dietrichs E. *The Cerebellum – Structure and Connections*. Vol 103. Elsevier B.V.; 2012. doi:10.1016/B978-0-444-51892-7.00001-2

2. Szulc KU, Lerch JP, Nieman BJ, et al. 4D MEMRI atlas of neonatal FVB/N mouse brain development. *NeuroImage*. 2015;118:49-62. doi:10.1016/j.neuroimage.2015.05.029

3. Sathyanesan A. Emerging connections between cerebellar development , behaviour and complex brain disorders. *Nat Rev Neurosci*. 2019;20(May). doi:10.1038/s41583-019-0152-2

4. Stoodley CJ. The Cerebellum and Neurodevelopmental Disorders. *The Cerebellum*. 2016;15:34-37. doi:10.1007/s12311-015-0715-3

5. Beekhof GC, Osorio C, White JJ, et al. Differential spatiotemporal development of Purkinje cell populations and cerebellum-dependent sensorimotor behaviors. *eLife*. Published online 2021:1-34.

6. Fatemi SH, Halt AR, Realmuto G, et al. Purkinje Cell Size is Reduced in Cerebellum of Patients With Autism. *Cell Mol Neurobiol*. 2002;22(2):171-175.

7. Tsai PT, Hull C, Chu Y, et al. Autistic-like behaviour and cerebellar dysfunction in Purkinje cell Tsc1 mutant mice. *Nature*. 2012;488(7413):647-651. doi:10.1038/nature11310

8. Cupolillo D, Hoxha E, Faralli A, et al. Autistic-Like Traits and Cerebellar Dysfunction in Purkinje Cell PTEN Knock-Out Mice. *Neuropsychopharmacology*. 2016;41:1457-1466. doi:10.1038/npp.2015.339

9. Yamashiro K, Hori K, Lai ESK, et al. AUTS2 Governs Cerebellar Development, Purkinje Cell Maturation, Motor Function and Social Communication. *iScience*. 2020;23(12):101820. doi:10.1016/j.isci.2020.101820

10. Kim J, Kwon N, Chang S, et al. Altered branching patterns of Purkinje cells in mouse model for cortical development disorder. *Sci Rep*. Published online 2011:1-7. doi:10.1038/srep00122

11. Robinson L, Guy J, Mckay L, et al. Morphological and functional reversal of phenotypes in a mouse model of Rett syndrome. *Brain*. 2012;135(January). doi:10.1093/brain/aws096

12. Usui N, Co M, Harper M, Rieger MA, Dougherty JD, Konopka G. Sumoylation of FOXP2 Regulates Motor Function and Vocal Communication Through Purkinje Cell Development. *Biol Psychiatry*. 2017;81(3):220-230. doi:10.1016/j.biopsych.2016.02.008

13. Sundberg M, Tochitsky I, Buchholz DE, et al. Purkinje cells derived from TSC patients display hypoexcitability and synaptic de fi cits associated with reduced FMRP levels and reversed by rapamycin. *Mol Psychiatry*. 2018;23:2167-2183. doi:10.1038/s41380-018-0018-4

14. Hwang WJ, Kwak YB, Cho KIK, et al. Thalamic Connectivity System Across Psychiatric Disorders : Current Status and Clinical Implications. *Biol Psychiatry Glob Open Sci*. 2022;2(4):332-340. doi:10.1016/j.bpsgos.2021.09.008

15. Krol A, Wimmer RD, Halassa MM, Feng G. Thalamic Reticular Dysfunction as a Circuit Endophenotype in Neurodevelopmental Disorders. *Neuron*. 2018;98(2):282-295. doi:10.1016/j.neuron.2018.03.021

16. Antón-Bolaños N, Espinosa A, Lopew-Bendito G. Developmental interactions between thalamus and cortex : a true love reciprocal story. *Curr Opin Neurobiol*. 2018;52:33-41. doi:10.1016/j.conb.2018.04.018

17. Sato H, Hatakeyama J, Iwasato T, Araki K. Thalamocortical axons control the cytoarchitecture of neocortical layers by specific supply of VGF. *eLife*. Published online 2022:1-23.

18. Fatemi SH, Folsom TD. The Neurodevelopmental Hypothesis of Schizophrenia, Revisited. *Schizophr Bull*. 2009;35(3):528-548. doi:10.1093/schbul/sbn187

19. Ismail FY, Shapiro BK. What are neurodevelopmental disorders ? *Curr Opin Neurol*. Published online 2019:611-616. doi:10.1097/WCO.0000000000000710

20. Qiu LR, Fernandes DJ, Szulc-Lerch KU, et al. Mouse MRI shows brain areas relatively larger in males emerge before those larger in females. *Nat Commun*. 2018;9(1). doi:10.1038/s41467-018-04921-2

21. Alexander DC, Dyrby TB, Nilsson M. Imaging brain microstructure with diffusion MRI : practicality and applications. *NMR Biomed*. 2019;32(September 2017):1-26. doi:10.1002/nbm.3841

22. Hüppi P. *"Diffusion Tensor Imaging in Brain Development" in Diffusion MRI: Theory, Methods, and Applications*. (Derek K. Jones P, ed.). Oxford Academic; 2010. doi:https://doi.org/10.1093/med/9780195369779.003.0030

23. Chokshi FH, Poretti A, Meoded A, Huisman TAGM. Normal and Abnormal Development of the Cerebellum and Brainstem as Depicted by Diffusion Tensor Imaging. *Semin Ultrasound CT MRI*. 2011;32(6):539-554. doi:10.1053/j.sult.2011.06.005

24. Zheng J, Yang Q, Makris N, et al. Three-Dimensional Digital Reconstruction of the Cerebellar Cortex: Lobule Thickness, Surface Area Measurements, and Layer Architecture. *Cerebellum*. 2023;22(2):249-260. doi:10.1007/s12311-022-01390-8

25. Ronen I, Valette J. Diffusion-Weighted Magnetic Resonance Spectroscopy. *eMagRes*. 2015;4(1):733-750. doi:10.1002/9780470034590.emrstm1471

26. Ligneul C, Döring A, Beaulieu C, et al. Diffusion-weighted MR spectroscopy : Consensus, recommendations ,and resources from acquisition to modeling. *Magn Reson Med*. 2024;(May 2023):860-885. doi:10.1002/mrm.29877

27. Palombo M, Ligneul C, Najac C, et al. New paradigm to assess brain cell morphology by diffusion-weighted MR spectroscopy in vivo. *Proc Natl Acad Sci U S A*. 2016;113(24):6671-6676. doi:10.1073/pnas.1504327113

28. Palombo M, Ligneul C, Valette J. Modeling Diffusion of Intracellular Metabolites in the Mouse Brain up to Very High Diffusion-Weighting : Diffusion in Long Fibers (Almost) Accounts for Non-Monoexponential Attenuation. *Magn Reson Med*. 2017;350(November 2016):343-350. doi:10.1002/mrm.26548

29. Ligneul C, Palombo M, Hernández-Garzón E, et al. Diffusion-weighted magnetic resonance spectroscopy enables cell-specific monitoring of astrocyte reactivity in vivo. *NeuroImage*. 2019;191(December 2018):457-469. doi:10.1016/j.neuroimage.2019.02.046

30. Genovese G, Millecamps A, Abdoulkader N, et al. Inflammation-driven glial alterations in the cuprizone mouse model probed with diffusion-weighted magnetic resonance spectroscopy at 11 . 7 T. *NMR Biomed*. 2021;(January):1-13. doi:10.1002/nbm.4480

31. Ercan E, Magro-checa C, Valabregue R, et al. Glial and axonal changes in systemic lupus erythematosus measured with diffusion of intracellular metabolites. *Brain*. 2016;139:1447-1457. doi:10.1093/brain/aww031

32. De Marco R, Ronen I, Branzoli F, et al. Diffusion-weighted MR spectroscopy (DW-MRS) is sensitive to LPS-induced changes in human glial morphometry : A preliminary study. *Brain Behav Immun*. 2022;99(October 2021):256-265.

33. Takeuchi Y, Asano H, Katayama Y, Muragaki Y, Imoto K, Miyata M. Large-Scale Somatotopic Refinement via Functional Synapse Elimination in the Sensory Thalamus of Developing Mice. *J Neurosci*. 2014;34(4):1258-1270. doi:10.1523/JNEUROSCI.3865-13.2014

34. Kumar R, Delshad S, Macey PM, Woo MA, Harper RM. Development of T2-relaxation values in regional brain sites during adolescence. *Magn Reson Imaging*. 2011;29(2):185-193. doi:10.1016/j.mri.2010.08.006

35. Tkac I, Rao R, Georgieff MK, Gruetter R. Developmental and Regional Changes in the Neurochemical Profile of the Rat Brain Determined by In Vivo 1 H NMR Spectroscopy. *Magn Reson Med*. 2003;32:24-32. doi:10.1002/mrm.10497

36. Tkáč I, Henry P gilles, Andersen P, Keene CD, Low WC, Gruetter R. Highly Resolved In Vivo 1 H NMR Spectroscopy of the Mouse Brain at 9 . 4 T. *Magn Reson Med*. 2004;484(December 2003):478-484. doi:10.1002/mrm.20184

37. Chahboune H, Ment LR, Stewart WB, et al. Hypoxic Injury during Neonatal Development in Murine Brain: Correlation between In Vivo DTI Findings and Behavioral Assessment. *Cereb Cortex*. 2009;19(12):2891-2901. doi:10.1093/cercor/bhp068

38. McKay BE, Turner RW. Physiological and morphological development of the rat cerebellar Purkinje cell. *J Physiol*. 2005;567(3):829-850. doi:10.1113/jphysiol.2005.089383

39. Beekhof GC, Osório C, White JJ, Zoomeren SV, Der HV. Differential spatiotemporal development of Purkinje cell populations and cerebellum-dependent sensorimotor behaviors. *eLife*. Published online 2019.

40. Madsen S, Ottersen OLEP, Storm-mathisen JON. IMMUNOCYTOCHEMICAL VISUALIZATION OF TAURINE: NEURONAL LOCALIZATION IN THE RAT CEREBELLUM. *Neurosci Lett*. 1985;60:255-260.

41. Magnusson KR, Madl JE, Clements JR, Wu JY, Larson AA, Beitz AJ. Colocalization of Taurine- and Cysteine Sulfinic Acid Decarboxylase- like Immunoreactivity in the Cerebellum of the Rat with Monoclonal Antibodies Against Taurine. *J Neurosci*. 1988;8(December).

42. Hussy N, Deleuze C, Desarménien MG, Moos FC. Osmotic regulation of neuronal activity: A new role for taurine and glial cells in a hypothalamic neuroendocrine structure. *Prog Neurobiol*. 2000;62(2):113-134. doi:10.1016/S0301-0082(99)00071-4

43. Aerts L, Van Assche FA. Taurine and taurine-deficiency in the perinatal period. *J Perinat Med*. 2002;30:281-286.

44. Ligneul C, Valette J. Probing metabolite diffusion at ultra-short time scales in the mouse brain using optimized oscillating gradients and "short"-echo-time diffusion-weighted MRS. *NMR Biomed*. 2017;30(1):1-10. doi:10.1002/nbm.3671

45. Cengiz P, Zafer D, Chandrashekhar JH, et al. Developmental differences in microglia morphology and gene expression during normal brain development and in response to hypoxia-ischemia. *Neurochem Int*. 2019;127(December 2018):137-147. doi:10.1016/j.neuint.2018.12.016

46. Bushong EA, Martone ME, Ellisman MH. Maturation of astrocyte morphology and the establishment of astrocyte domains during postnatal hippocampal development. *Int J Dev Neurosci*. 2004;22(2):73-86. doi:10.1016/j.ijdevneu.2003.12.008

47. Somaiya RD, Huebschman NA, Chaunsali L, et al. Development of astrocyte morphology and function in mouse visual thalamus. *J Comp Neurol*. 2022;530(7):945-962. doi:10.1002/cne.25261

48. Clavreul S, Abdeladim L, Hernández-Garzón E, et al. Cortical astrocytes develop in a plastic manner at both clonal and cellular levels. *Nat Commun*. 2019;10(1):1-14. doi:10.1038/s41467-019-12791-5

49. Hernández-Benítez R, Pasantes-Morales H, Torres Saldaña I, Ramos-Mandujano G. Taurine stimulates proliferation of mice embryonic cultured neural progenitor cells. *J Neurosci Res*. 2010;88(8):1673-1681. doi:10.1002/jnr.22328

50. Mersman B, Zaidi W, Syed NI, Xu F. Taurine Promotes Neurite Outgrowth and Synapse Development of Both Vertebrate and Invertebrate Central Neurons. *Front Synaptic Neurosci*. 2020;12(July):1-18. doi:10.3389/fnsyn.2020.00029

51. Hüppi PS, Posse S, Lazeyras F, Burri R, Bossi E, Herschkowitz N. Magnetic resonance in preterm and term newborns:1H-spectroscopy in developing human brain. *Pediatr Res*. 1991;30(6):574-578. doi:10.1203/00006450-199112000-00017

52. Pouwels PJW, Brockmann K, Kruse B, et al. Regional Age Dependence of Human Brain Metabolites from Infancy to Adulthood as Detected by Quantitative Localized Proton MRS. *Pediatr Res*. 1999;46(4):474-474. doi:10.1203/00006450-199910000-00019

53. Sturman JA, Rassin DK, Gaull GE, Cote LJ. Taurine in Developing Rhesus Monkey Brain. *J Neurochem*. 1980;35(2):304-310. doi:10.1111/j.1471-4159.1980.tb06265.x

54. Emir UE, Auerbach EJ, van de Moortele PF, et al. Regional neurochemical profiles in the human brain measured by 1H MRS at 7T using local B 1 shimming. *NMR Biomed*. 2012;25(1):152-160. doi:10.1002/nbm.1727

55. Fukumitsu K, Hatsukano T, Yoshimura A, Heuser J. Mitochondrial fission protein Drp1 regulates mitochondrial transport and dendritic arborization in cerebellar Purkinje cells. *Mol Cell Neurosci*. 2016;71:56-65. doi:10.1016/j.mcn.2015.12.006

56. Jayabal S, Ljungberg L, Watt AJ. Transient cerebellar alterations during development prior to obvious motor phenotype in a mouse model of spinocerebellar ataxia type 6. *J Physiol*. 2017;3:949-966. doi:10.1113/JP273184

57. Chen XR, Heck N, Lohof AM, et al. Mature Purkinje Cells Require the Retinoic Acid-Related Orphan Receptor- alpha-ROR alpha to Maintain Climbing Fiber Mono-Innervation and Other Adult Characteristics. *J Neurosci*. 2013;33(22):9546-9562. doi:10.1523/JNEUROSCI.2977-12.2013

58. Hetsch F, Wang D, Chen X, et al. CKAMP44 controls synaptic function and strength of relay neurons during early development of the dorsal lateral geniculate nucleus. *J Physiol*. 2022;15:3549-3565. doi:10.1113/JP283172

59. Ligneul C, Palombo M, Valette J. Metabolite diffusion up to very high b in the mouse brain in vivo: Revisiting the potential correlation between relaxation and diffusion properties. *Magn Reson Med*. 2017;77(4):1390-1398. doi:10.1002/mrm.26217

60. Ligneul C, Andersson J, Jbabdi S, Lerch J, Clarke WT. Rejecting or retaining motion corrupted transients in di ff usion- weighted MRS : high b-values and multiple directions. In: *Proc. Intl. Soc. Mag. Reson. Med. 31 (2023)*. Vol 31. ; 2023:3934.

61. Coupé P, Yger P, Prima S, Hellier P, Kervrann C, Barillot C. An Optimized Blockwise Nonlocal Means Denoising Filter for 3-D Magnetic Resonance Images. *IEEE Trans Med Imaging*. 2008;27(4):425-441.

62. Goerzen D, Fowler C, Devenyi GA, et al. An MRI-Derived Neuroanatomical Atlas of the Fischer 344 Rat Brain. *Sci Rep*. 2020;10:1-13. doi:10.1038/s41598-020-63965-x

63. Friedel M, Eede MCV, Pipitone J, Chakravarty MM, Lerch JP. Pydpiper : a flexible toolkit for constructing novel registration pipelines. *Front Neuroinformatics*. 2014;8(July):1-21. doi:10.3389/fninf.2014.00067

64. Marchadour C, Brouillet E, Hantraye P, Lebon V, Valette J. Anomalous diffusion of brain metabolites evidenced by diffusion-weighted magnetic resonance spectroscopy in vivo. *J Cereb Blood Flow Metab*. 2012;32(August). doi:10.1038/jcbfm.2012.119

65. Kuznetsova A. lmerTest Package : Tests in Linear Mixed Effects Models. *J Statis*. 2017;82(13). doi:10.18637/jss.v082.i13